https://doi.org/10.5194/egusphere-2025-5185
Preprint. Discussion started: 5 December 2025

Retrieval of Global Aerosol and Surface Properties from the Gaofen-5 Directional Polarimetric Camera Measurements

Zhenyu Zhang[1], Jing Li[1], Yueming Dong[1], Chongzhao Zhang[1], Qiurui Li[1], and Ling Gao[2]

[1]Department of Atmospheric and Oceanic Sciences, School of Physics, Peking University, 100871, Beijing, China
[2]National Satellite Meteorological Center, China Meteorological Administration, 100081, Beijing, China

Correspondence: Jing Li (jing-li@pku.edu.cn)

Abstract.

Multi-angle polarimetry has been recognized as the most effective configuration to retrieve aerosol parameters from space. In this study, we developed a numerical inversion algorithm that simultaneously retrieves aerosol optical depth (AOD), single scattering albedo (SSA), and land surface albedo (expressed as the Directional Hemispherical Reflectance, DHR) from multi-angle polarimetric observations of China's Directional Polarimetric Camera (DPC) onboard the Gaofen-5 satellite. As one of the few multi-angle polarimetric sensors in operation, DPC provides multi-spectral polarized radiance measurements at up to 12 viewing angles, offering unique advantages for retrieving multiple aerosol parameters. With sensitivity experiments using the VLIDORT radiative transfer model, we first clarified that SSA retrieval with an uncertainty of 0.03 requires degree of linear polarization (DOLP) observation uncertainties below 0.01 with carefully designed viewing geometries. Subsequently, an optimization-based algorithm was implemented to minimize discrepancies between simulated and observed multi-angle scalar reflectance and DOLP. The algorithm performs well on the simulated dataset, with correlation coefficients of 440 nm DHR, AOD, and SSA (when AOD $>$ 0.4) reaching 0.9, 0.8, and 0.7, respectively. Retrieval using DPC measurements and validation against AERONET observation also demonstrated robust performance. Retrieved 440 nm AOD achieved a correlation coefficient of 0.75 with AERONET, comparable to operational satellite products such as those from MODIS. The correlation coefficient of 440 nm SSA under high aerosol loading (AOD $>$ 0.4) is 0.38, matching the precision of Polarization and Directionality of the Earth's Reflectances instrument (POLDER) SSA products, the previous best satellite-based SSA products. Regional and global results captured spatiotemporal aerosol variability of typical pollution events, including biomass burning plumes and dust transport tracks. The DHR results also align closely with MODIS-derived DHR (bias = 0.001). This work not only advances DPC's capability for comprehensive aerosol characterization globally, but also provides a physically interpretable framework for global aerosol and surface monitoring.

1 Introduction

Aerosol properties are of significant importance in both climate change research and atmospheric environmental studies (Albrecht, 1989; Ramanathan et al., 2001; Li et al., 2022a). Satellite remote sensing has emerged as a critical tool for acquiring comprehensive global aerosol observations (Dubovik et al., 2019; Liu et al., 2021). Over the past decades, numerous space-

https://doi.org/10.5194/egusphere-2025-5185
Preprint. Discussion started: 5 December 2025

borne sensors have been employed for global aerosol observation, providing long-term data that serve as crucial references for estimating aerosol radiative effects (Diner et al., 1998; Mishchenko et al., 2007; Torres et al., 2007; Dubovik et al., 2011; Levy et al., 2013). Earlier sensors, such as MODIS, primarily offered single-angle scalar observations for each pixel with limited information content, typically only capable of retrieving column loading of aerosols (Aerosol Optical Depth, AOD) while requiring assumed surface reflectance and other aerosol properties such as Single Scattering Albedo (SSA) which reflects the scattering and absorbing properties of aerosols (Levy et al., 2007b, 2013).

Recently, multi-angle polarimetric sensors could provide both intensity and polarization measurements of radiation at multiple viewing angles for individual pixels, significantly enhancing the information available for the retrieval of aerosol parameters (Dubovik et al., 2019). The multi-angle observations facilitate the separation of surface and aerosol contributions, while polarization signals exhibit heightened sensitivity to aerosol scattering and absorbing properties (Dong et al., 2024). Consequently, multi-angle polarimetric observations have emerged as one of the most promising satellite remote sensing techniques for retrieving a series of aerosol and surface parameters on a global scale (Mishchenko and Travis, 1994; Mishchenko et al., 2010). This potential has been demonstrated by algorithms developed for the world's first operational spaceborne multi-angle polarimetric sensor, Polarization and Directionality of the Earth's Reflectances instrument (POLDER), which achieved comprehensive retrieval of multiple parameters including AOD, SSA, and surface reflectance (Chen et al., 2020; Dubovik et al., 2011; Hasekamp et al., 2011, 2024; Li et al., 2019). These achievements underscore the significant capability of multi-angle polarimetric sensors in advancing aerosol remote sensing. Following POLDER's retirement in 2013, there was a gap in operational multi-angle polarimetric satellite sensors until the launch of the Directional Polarimetric Camera (DPC) aboard Gaofen-5 in 2018 (Li et al., 2018). The DPC has since provided valuable multi-angle polarimetric observations, facilitating SSA retrieval in recent years.

The DPC has eight spectral channels spanning 443–910 nm and can provide up to 12 viewing angles, with three channels (490, 670, and 865 nm) offering measurements of both Q and U linear polarization components, theoretically enabling SSA retrieval (Li et al., 2018). However, existing aerosol retrievals based on DPC observations have primarily focused on AOD, achieving correlation coefficients of up to 0.9 with ground-based measurements (Wang et al., 2021; Jin et al., 2022; Ge et al., 2022). Large-scale SSA retrieval studies using DPC observations remain limited. Fang et al. (2022) applied the RemoTAP algorithm (previously used for POLDER SSA retrieval) to DPC observations to retrieve AOD, fine mode AOD, and SSA over eastern China. Their results showed a correlation coefficient of 0.45 between retrieved SSA and AERONET measurements when 670 nm AOD exceeded 0.3. Similarly, Jin et al. (2024) implemented the GRASP algorithm for oceanic SSA retrieval from DPC observations. Additionally, Dong et al. (2024) employed machine learning methods to retrieve global land SSA from DPC observations and yielded promising results. Nevertheless, machine learning approaches often lack physical interpretability, while numerical methods have so far been limited to regional and oceanic applications. This highlights the need for further exploration of global SSA retrieval using DPC observations.

This study develops a numerical inversion algorithm based on DPC's multi-angle polarimetric observations to retrieve global AOD, SSA, and surface parameters, offering insights into global aerosol and surface properties in recent years.

https://doi.org/10.5194/egusphere-2025-5185
Preprint. Discussion started: 5 December 2025

2 Data and Methods

2.1 DPC Measurements

DPC is China's first operational spaceborne multi-angle polarimetric sensor, successively launched on the Gaofen-5 satellite in May 2018, on Gaofen-5(02) satellite in 2021, and on Daqi-1 satellite in 2022, respectively (Dai et al., 2024; Li et al., 2022b). This study uses measurements from the first DPC sensor since data is not well calibrated for the following two sensors. The DPC features a spatial resolution of 3.3 km and achieves multi-angle observations of the same target through along-track scanning, with up to 12 viewing angles (typically exceeding 9 angles) for most pixels. The sensor provides measurements across 8 spectral bands from visible to near-infrared wavelengths, including polarized observations at 490, 670, and 865 nm.

The laboratory calibration errors of DPC are within 5 % for normalized radiation and within 0.02 for the degree of linear polarization (DOLP) measurements (Li et al., 2018). However, after launch, the sensors experienced instrumental drift, leading to a significant increase in measurement errors. Studies show potential radiometric drift up to 23 % (Zhu et al., 2022) and DOLP errors possibly exceeding 0.04 (Qie et al., 2021). This study thus employs the Rayleigh scattering-based correction coefficients developed by Zhu et al. (2022) to calibrate DPC's scalar radiance observations at 443, 490, 565, and 670 nm bands, which are subsequently used for AOD, SSA, and Directional Hemispherical Reflectance (DHR) retrievals. The correction capability decreases with increasing wavelength due to the rapid diminishment of Rayleigh scattering contributions, with theoretical correction errors of approximately 2 % at 443 nm, 4 % at 565 nm, and 7 % at 670 nm. The 865 nm band remains uncorrected due to negligible Rayleigh scattering. In this study, aerosol and surface parameter retrieval is confined to the corrected observations from the four calibrated bands (443, 490, 565, and 670 nm), and the screening of cloud/ice/snow pixels additionally employs the original measurements from the other bands.

2.2 Auxiliary Data

Some auxiliary data are needed to characterize surface reflectance and other related processes. Prior to the inversion process, we matched these auxiliary data with DPC observations. Specifically, for land surface, monthly 0.05° NDVI data from MODIS/Aqua observations are matched to calculate surface polarized reflectance. For water surfaces, hourly 0.25° ERA5 global wind speed and wind direction data (Hersbach et al., 2020), monthly ocean salinity data from the GLBu0.08 dataset (Cummings and Smedstad, 2013), and monthly averaged 4 km resolution chlorophyll concentration products from MODIS/Aqua observations are matched to compute the surface reflectance (O'Reilly and Werdell, 2019). Considering the relatively minor influence of aerosol phase matrices on the inversion (Su et al., 2021; Zhang et al., 2024), the phase matrices from the aerosol models clustered by Levy et al. (2007a) are utilized in the retrieval. This approach ensures comprehensive representation of surface and atmospheric conditions, enhancing the accuracy and reliability of the retrieval process.

https://doi.org/10.5194/egusphere-2025-5185
Preprint. Discussion started: 5 December 2025

2.3 AERONET AOD and SSA

The AERONET is a ground-based aerosol remote sensing network, providing long-term observations of aerosol optical and microphysical properties, covering most of the continental areas around the world (Holben et al., 1998). The AERONET AOD observations are derived from direct solar radiation and the SSA products are retrieved from diffuse sky radiance (Dubovik and King, 2000). The AOD measurements can be obtained at several wavelengths ranging from 340 nm to 1640 nm, whereas the SSA products can be obtained at four wavelengths at 440, 675, 870 and 1020 nm. These products are very accurate with an AOD uncertainty of 0.01 (visible)–0.02 (UV) and an SSA uncertainty of 0.03 (Giles et al., 2019; Sinyuk et al., 2020), and are often used to validate satellite products. However, as the quality control of level 2.0 inversion products requires AOD > 0.4, many stations do not have extensive level 2.0 SSA records. Considering the data quality and data availability, we utilize the all-point Version 3 Level 2.0 direct AOD measurements and quality-controlled Level 1.5 almucantar inversion SSA products in this work. The quality-controlled Level 1.5 SSA are firstly derived from Level 1.5 observations by applying all the Level 2.0 quality control criteria except the AOD threshold (e.g., SZA $> 50°$, sky error < 5 %, and coincident Level 2.0 AOD measurements). In subsequent sections, different AOD thresholds were applied for screening purposes.

2.4 MODIS Albedo

Since AERONET does not retrieve surface albedo, the validation of the DPC retrieved surface parameters is performed using the daily surafce products from the MCD43C1 dataset which are derived from MODIS/Terra and MODIS/Aqua observations (Schaaf et al., 2002). The MCD43C1 dataset utilizes the RossThick-LiSparse (RTLS) kernel-driven model to characterize land surface reflectance (Schaaf et al., 2002), which can be represented as:

$$R_\lambda(\theta_0,\theta,\phi) = K_{iso}(\lambda) + K_{vol} f_{vol}(\theta_0,\theta,\phi) + K_{geo} f_{geo}(\theta_0,\theta,\phi) \tag{1}$$

In Eq. 1, the terms $K_{iso}(\lambda)$, $K_{vol}(\lambda)f_{vol}$ and $K_{geo}(\lambda)f_{geo}$ represent isotropic, volumetric, and geometric-optical surface scattering at wavelength λ, respectively. Here, $K_{iso}(\lambda)$, $K_{vol}(\lambda)$, and $K_{geo}(\lambda)$ are the spectral intensity parameters of the three components, while $f_{vol}(\theta_0,\theta,\phi)$ and $f_{geo}(\theta_0,\theta,\phi)$ are Ross-thick and Li-sparse kernel functions, respectively. In our retrieval algorithm, we utilize the wavelength-dependent RTLS model (Litvinov et al., 2011), which can expressed as:

$$R_\lambda(\theta_0,\theta,\phi) = K(\lambda)[1 + k_{vol} f_{vol}(\theta_0,\theta,\phi) + k_{geo} f_{geo}(\theta_0,\theta,\phi)] \tag{2}$$

where $K(\lambda)$ is a wavelength dependent intensity parameter, whereas k_{vol} and k_{geo} are wavelength independent parameters. The terms $k_{vol}K(\lambda)$ and $k_{geo}K(\lambda)$ in Eq. 2 correspond to $K_{vol}(\lambda)$ and $K_{geo}(\lambda)$ in Eq. 1, respectively.

In this study, the Directional Hemispherical Reflectance (DHR, also known as black sky albedo), which represents surface albedo in the absence of atmospheric scattering effects, is computed using the three intensity parameters of the RTLS model (Sinyuk et al., 2007). Considering the differences in the spectral bands between MODIS and DPC observations, the DHR from MODIS is linearly interpolated to the wavelengths of DPC channels. The accuracy of DPC's surface parameter retrievals is evaluated by comparing the retrieved DHR with interpolated MODIS DHR.

https://doi.org/10.5194/egusphere-2025-5185
Preprint. Discussion started: 5 December 2025

2.5 VLIDORT Radiative Transfer Model

The Vector LInearized Discrete Ordinate Radiative Transfer (VLIDORT) model is a vector radiative transfer model that accounts for multiple scattering in real atmospheres. It accurately simulates Stokes vectors and their linearized matrices (Jacobians) at arbitrary altitudes and viewing geometries, providing high-precision radiative simulations for satellite remote sensing applications and serving as an effective forward model in numerical inversion algorithms (Spurr, 2006). The model allows user-defined atmospheric layering with customizable layer heights and optical properties (including total optical depth, SSA, and Legendre expansion coefficients of phase matrix for both aerosols and gases). It calculates output radiation at selected layers and viewing angles along with corresponding Jacobian matrices with respect to surface parameters and the three key atmospheric optical parameters: AOD, SSA, and phase matrix expansion coefficients. In this study, VLIDORT was employed for sensitivity experiments and served as the forward model in the numerical inversion algorithm.

2.6 Retrieval algorithm

Polarimetric multi-angle observations provide both polarization and angular information, enabling the retrieval of multiple parameters such as AOD, SSA, and surface reflectance from a single pixel. However, the system is strongly nonlinear and high-dimensional, thus the inverse problem is very difficult to solve analytically and should be addressed using iterative numerical approaches.

The relationship between satellite observations and the parameters to be retrieved can be expressed as:

$$\mathbf{y} = \mathbf{F}(\mathbf{x}) + \varepsilon \tag{3}$$

where $\mathbf{y}$ represents the satellite observations, such as the Stokes vectors at various bands and viewing angles; $\mathbf{x}$ is the state vector, which includes the parameters to be retrieved, such as AOD, SSA, and surface reflectance; $\mathbf{F}$ is the forward model, also known as the observation operator, which maps the state vector to the observation space, and is often represented by a radiative transfer model in aerosol retrieval algorithms; and ε is the error term, encompassing both observation uncertainties and forward model uncertainties. Numerical inversion aims to find a state vector $\mathbf{x^a}$ such that $\mathbf{F}(\mathbf{x^a})$ closely matches $\mathbf{y}$, with $\mathbf{x^a}$ being the final retrieval result.

The cost function is constructed as:

$$J(\mathbf{x}) = \frac{1}{2}\left[\mathbf{y} - \mathbf{F}(\mathbf{x})\right]^{\mathrm{T}} \mathbf{S}_{\epsilon}^{-1}\left[\mathbf{y} - \mathbf{F}(\mathbf{x})\right] + \frac{1}{2}\left(\mathbf{x} - \mathbf{x}_0\right)^{\mathrm{T}} \mathbf{S}_a^{-1}\left(\mathbf{x} - \mathbf{x}_0\right) \tag{4}$$

where $\mathbf{S}_{\epsilon}$ is the covariance matrix of observation errors, $\mathbf{x_0}$ is the vector of a priori estimates, and $\mathbf{S}_a$ is the covariance matrix of the errors in a priori estimates. The process of solving for $\mathbf{x^a}$ based on optimization theory involves minimizing $J(\mathbf{x})$. This minimization is achieved through iterative methods, with the direction of each iteration determined by the gradient descent of $J(\mathbf{x})$:

$$\nabla_{\mathbf{x}} J(\mathbf{x}) = -\mathbf{K}^{\mathrm{T}} \mathbf{S}_{\epsilon}^{-1}\left[\mathbf{y} - \mathbf{F}(\mathbf{x})\right] + \mathbf{S}_a^{-1}\left(\mathbf{x} - \mathbf{x}_0\right) \tag{5}$$

https://doi.org/10.5194/egusphere-2025-5185
Preprint. Discussion started: 5 December 2025

Here, $\mathbf{K}$ is the Jacobian matrix of $\mathbf{F}(\mathbf{x})$, representing the partial derivatives of $\mathbf{F}(\mathbf{x})$ with respect to the components of $\mathbf{x}$:

$$\mathbf{K}_{i,j} = \frac{\partial f_i(\mathbf{x})}{\partial x_j} \tag{6}$$

This iterative approach ensures that the retrieval process converges to a solution that optimally balances the observational data and a priori knowledge, providing robust estimates of the target parameters.

This study retrieves AOD, SSA, and kernel intensity parameters ($K(\lambda)$, k_{vol}, and k_{geo} in Eq. 2) of land surface models simultaneously. The wavelength-dependent RTLS model is utilized to parameterize land surface scalar reflectance, and the BPDF-NDVI model is used for polarized surface reflectance estimation (Litvinov et al., 2011; Maignan et al., 2009). For water surfaces, the New Cox-Munk model is implemented to compute the surface reflectance (Spurr, 2006). In this study, the a priori values are initially assigned as fixed constants to evaluate the algorithm's inherent retrieval capability, while also allowing for the use of multi-year averages from climate models or other observational products to improve performance. An overview of the retrieval algorithm is illustrated in Fig. 1, which mainly involves the following three steps:

(1) Data preprocessing. This involves three primary operations: calibration of DPC scalar observations, removing cloud/ice/snow pixels (Dong et al., 2024), and matching auxiliary data (including NDVI, wind speed, salinity, and chlorophyll concentration) with DPC observations.

(2) Iterative inversion. The calibrated and screened DPC observations, matched auxiliary data, and a priori estimates of target parameters are then fed into the VLIDORT radiative transfer model for iterative inversion. The algorithm minimizes the cost function of equation 4 to obtain the final retrieval results.

(3) Data post-processing. The retrieved parameters would be screened for further validation and mapping.

2.7 Sensitivity Experiment

To assess an important advantage of multi-angle polarimetry, the capability of SSA retrieval, we first investigate the sensitivity of both scalar and polarized reflectance to SSA. A series of radiative transfer simulations using the VLIDORT model for several DPC channels (443, 490, 565, 670, and 865 nm) under varying geometric parameters was conducted. By perturbing SSA within the AERONET precision (± 0.03) under a given set of aerosol and surface models, we analyzed changes in top-of-atmosphere (TOA) scalar and polarized reflectance to evaluate the sensitivity of outgoing radiation to SSA. The 0.03 SSA variation in our sensitivity analysis was chosen for two reasons. First, it corresponds to the reported uncertainty of precise AERONET SSA products, which often serve as a benchmark for validating satellite retrievals (Dubovik et al., 2000; Sinyuk et al., 2020). Second, the requirement to constrain aerosol radiative forcing in climate studies necessitates an SSA uncertainty below 0.03 (GCOS, 2016; Popp et al., 2016). Consequently, this accuracy represents a target for satellite remote sensing of SSA, which has not been met by most available products.

The sensitivity experiments employed the moderately absorbing aerosol model characterized by Levy et al. (2007a) for two distinct surface types, namely vegetation and bare soil, as described by Litvinov et al. (2011). These simulations aim to reveal the observation accuracy required for accurate SSA retrieval from multi-angle polarimetric measurements, and provide guidance for the design of viewing angle.

https://doi.org/10.5194/egusphere-2025-5185
Preprint. Discussion started: 5 December 2025

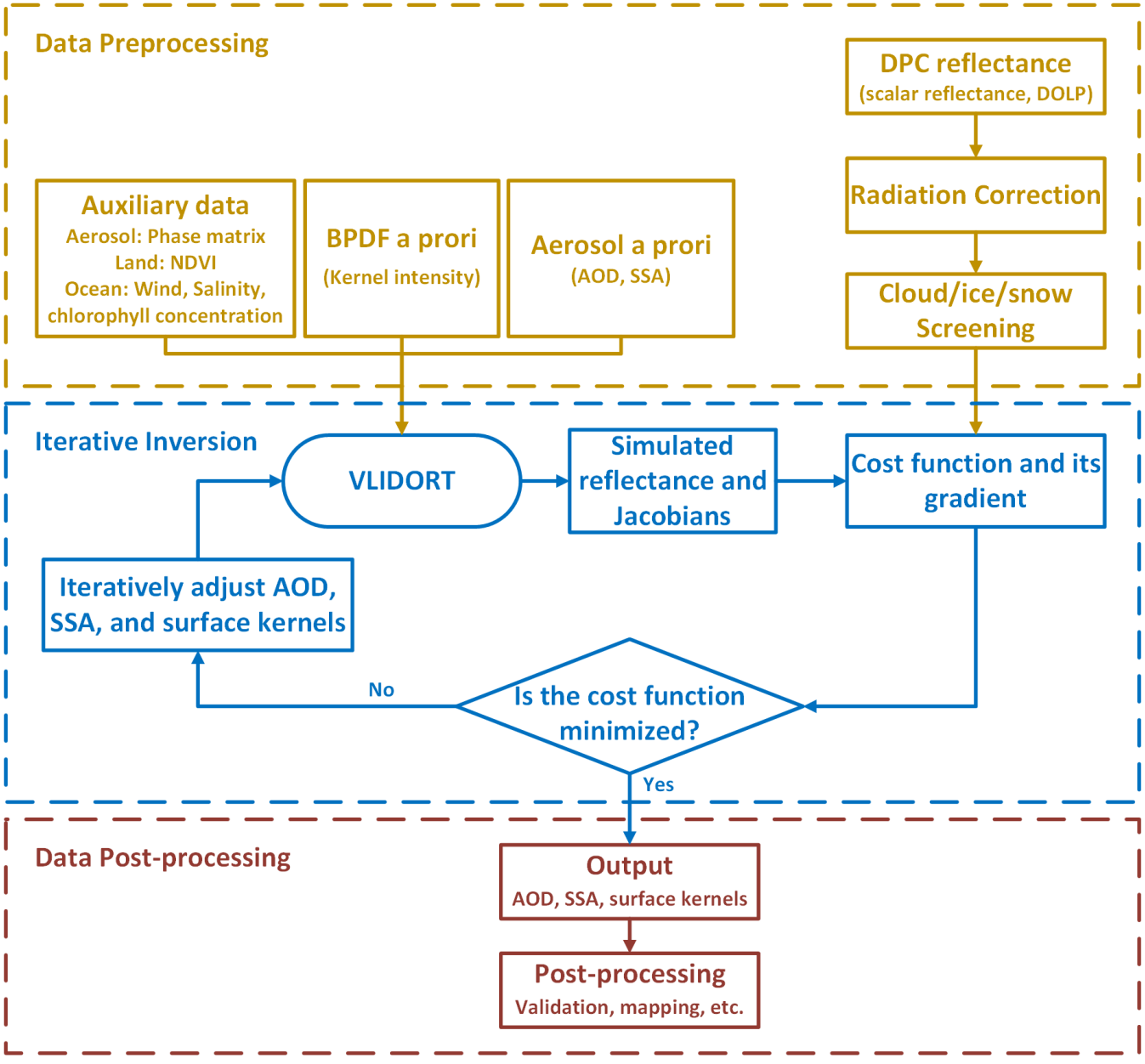

Figure 1. Flowchart for the DPC retrieval algorithm.

2.8 Retrieval Experiment Using Simulated Data

Before applying the retrieval algorithm to DPC observations, we conducted a series of retrieval experiments using simulated data to validate the performance of the algorithm. Since the uncertainties of DPC measurement largely exceed laboratory calibration results and are difficult to quantify (Qie et al., 2021; Zhu et al., 2022), the advantage of simulated datasets lies in

https://doi.org/10.5194/egusphere-2025-5185
Preprint. Discussion started: 5 December 2025

their controllable radiative errors and the elimination of model uncertainties. The simulated dataset was constructed based on a sampling of AERONET observations spatially and temporally matched with DPC measurements to better represent DPC observed conditions. Given that the majority of AERONET stations are located over land, the validation in this study primarily focuses on the retrieval performance for land aerosol and surface parameters. To construct the simulated dataset, DPC observations were first matched with AERONET measurements and MODIS surface parameters (RTLS parameters and NDVI) around the station. Subsequently, a sampling of these matched results was performed, and the sampled AOD, SSA, and surface parameters were used as "true values" to generate TOA scalar and polarized reflectances via VLIDORT simulations. These simulated reflectances were then treated as satellite observations and fed into the retrieval algorithm to retrieve aerosol and surface parameters. Finally, the retrieved parameters were compared with the "true values" used in the simulation to evaluate the inherent retrieval capability of the algorithm. This approach ensures a controlled assessment of the algorithm's performance while minimizing uncertainties arising from the lack of knowledge about actual observational errors.

2.9 Validation of the Retrieval Results

After conducting the sensitivity experiment and the retrieval experiment using simulated data, we applied the retrieval algorithm to DPC observations to derive global AOD, SSA, and DHR. The retrieved products were then systematically evaluated at three spatial scales to assess the algorithm's effectiveness with DPC observations and characterize spatiotemporal variations of aerosol and surface properties. At site scale, the retrieved parameters were spatiotemporally matched with AERONET ground-based measurements for validation. We averaged the retrieved parameters within an 8 km radius of each AERONET station. The AERONET AOD data was selected and averaged within a 30-minute window around the DPC overpass, whereas the AERONET daily SSA data was applied to compare against the retrievals. Several widely used statistical indicators, including the correlation coefficient (R), the linear regression equation (slope and intercept), the bias, and the root-mean-square error (RMSE), were considered for validation. The regional-scale analysis focused on the algorithm's capability to detect and characterize specific pollution events, including biomass burning episodes and dust outbreaks. Globally, we examined the spatiotemporal patterns of AOD, SSA, and DHR to assess their consistency with known atmospheric processes and surface characteristics.

3 Results

3.1 Sensitivity of Scalar and Polarimetric Measurements to SSA

Figures 2 and 3 illustrate the relative changes in TOA scalar reflectance (ΔI) and the changes in DOLP (ΔDOLP) respectively when the SSA varies by ± 0.03 under an aerosol loading of $\mathrm{AOD}_{550} = 0.5$. The angular dependence of ΔI and ΔDOLP exhibits comparable behavior for the two different surface types across most bands. Despite minor differences in magnitude and angular distribution at 670 nm, the overall trends are consistent. This consistency indicates that ΔI and ΔDOLP are not sensitive to surface parameters under SSA perturbations. For all five bands, ΔI has the same sign as ΔSSA, suggesting that

https://doi.org/10.5194/egusphere-2025-5185
Preprint. Discussion started: 5 December 2025

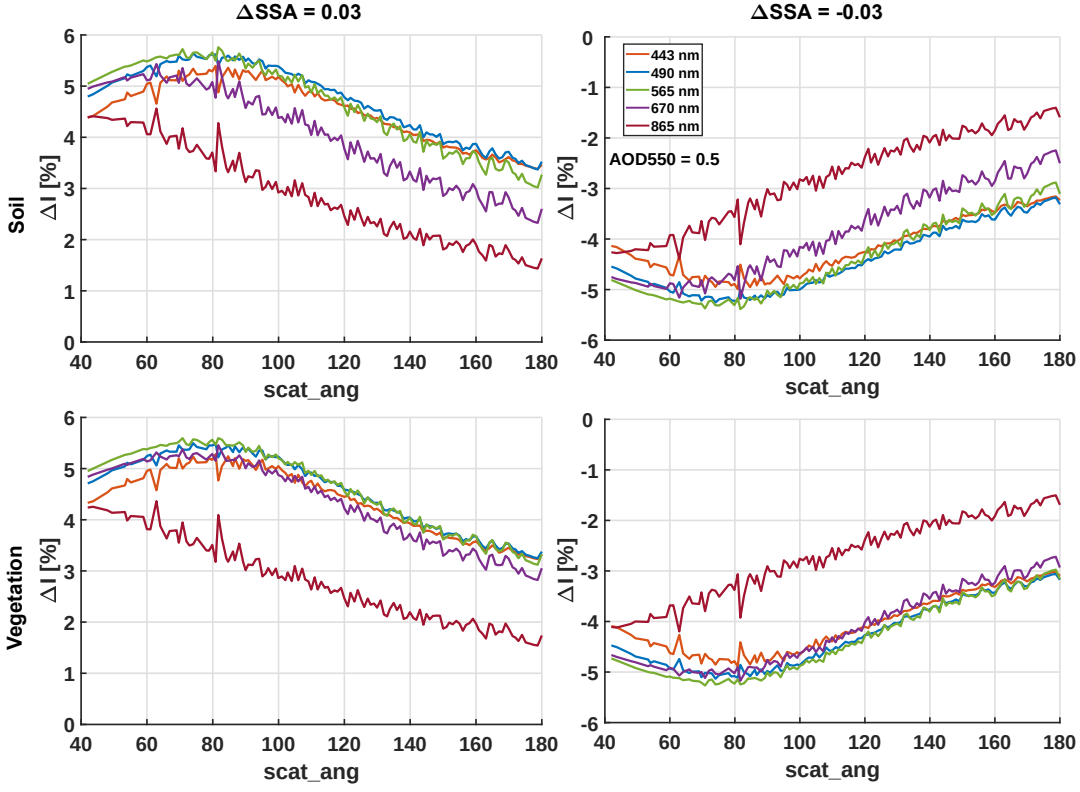

Figure 2. Relative changes in TOA scalar reflectance when the SSA varies by 0.03 (left) and -0.03 (right) under an aerosol loading of $\mathrm{AOD}_{550} = 0.5$ with bare soil (top) and vegetation (bottom) surface type.

an increase (or decrease) in SSA would lead to an increase (or decrease) in scalar reflectance. This aligns with the relationship between SSA and aerosol scattering, thereby affecting scalar reflectance. Generally, ΔI shows a slight increase as the angle decreases, particularly near $80°$. As the scattering angle approaches $180°$, ΔI approaches zero, becoming less sensitive to SSA.

ΔDOLP also varies with scattering angle, but its response to SSA differs by wavelength (Fig. 3). Similar to ΔI, at scattering angles near $180°$, ΔDOLP becomes negligible, indicating low sensitivity to SSA. For the three shorter wavelengths (443, 490, and 565 nm), ΔDOLP exhibits an opposite sign to ΔSSA, decreasing (increasing) with an increase (decrease) in SSA. As the scattering angle decreases from $180°$, ΔDOLP first increases and then decreases, reaching its maximum around $90°$. Within the scattering angle range of $60°$–$140°$, ΔDOLP remains above 0.005 and is relatively sensitive to SSA variations in this range. As the scattering angle further decreases, the magnitude of ΔDOLP also diminishes. The 865 nm band shows negligible ΔDOLP, suggesting minimal sensitivity to SSA at longer wavelength. The behavior of ΔDOLP for the 670 nm band is generally similar to that of the 443, 490, and 565 nm bands, except that ΔDOLP undergoes a sign reversal near $100°$. It should be noted that the relationship between ΔDOLP and scattering angle shown in Fig. 3 is based on conditions of $\mathrm{AOD}_{550} = 0.5$ and $\Delta\mathrm{SSA} = \pm 0.03$. Under different aerosol conditions, ΔDOLP may exhibit variations, but the overall trend

https://doi.org/10.5194/egusphere-2025-5185
Preprint. Discussion started: 5 December 2025

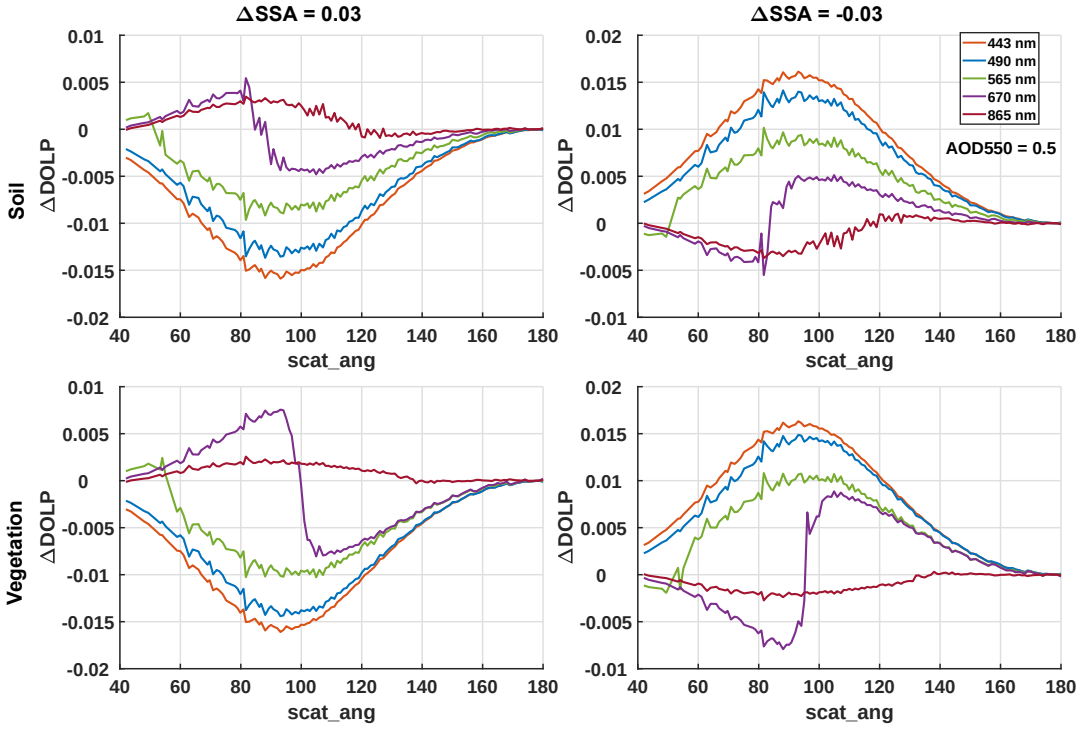

Figure 3. Same as Fig. 2, but for the changes in DOLP.

remains similar (Fig. 4). Specifically, shorter wavelengths show more pronounced changes in DOLP, and ΔDOLP follows a more consistent pattern with respect to scattering angle.

It is important to consider the magnitudes of ΔI and ΔDOLP when SSA varies by ± 0.03, as they reflect the required observational precision to achieve accurate SSA retrievals with uncertainties of 0.03. Under both vegetation and bare soil conditions with $\mathrm{AOD}_{550} = 0.5$, the magnitudes of ΔI across all bands and scattering angles are generally within 5 %. This range aligns with the typical scalar observation uncertainties of spaceborne sensors, including those of DPC, suggesting that retrieving SSA with 0.03 uncertainty is challenging under a scalar observation uncertainty of 5 %. The values of ΔDOLP are even smaller, with the most sensitive bands showing a change of only 0.01 at 90°. This implies that an SSA retrieval with an uncertainty of 0.03 requires a DOLP precision of 0.01, with additional constraints on observation angles. Considering that the laboratory calibration uncertainty of DPC's DOLP measurements is already 0.02, and accounting for potential instrument drift after launch, the actual observational uncertainty may exceed 0.04, according to our experiment, it is very difficult to obtain high quality SSA retrieval from DPC observations. However, since DPC's observational uncertainties and required precision are roughly of the same order of magnitude, its measurements can still be used for SSA retrieval to a certain extent, although with reduced precision.

Finally, the magnitudes of ΔI and ΔDOLP also depend on the AOD value. Figure 4 illustrates the variations of ΔI and ΔDOLP with scattering angle under different AOD conditions when SSA increases by 0.03 under the vegetation surface

https://doi.org/10.5194/egusphere-2025-5185
Preprint. Discussion started: 5 December 2025

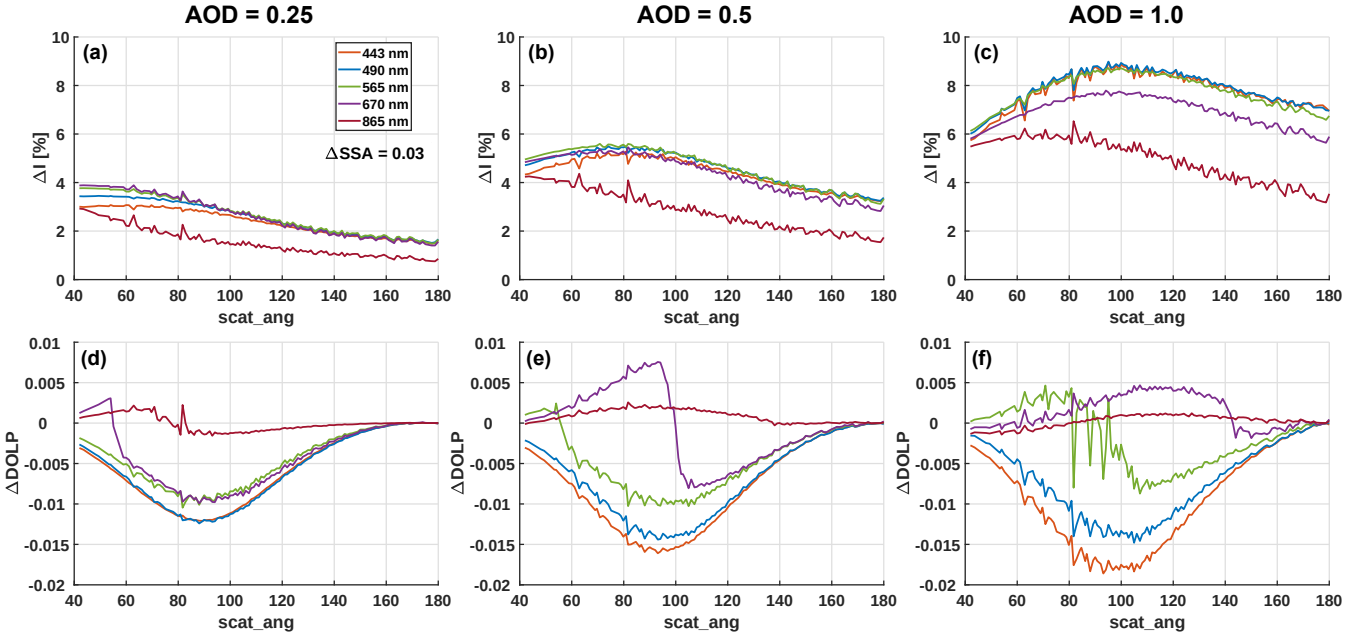

Figure 4. Relative changes in TOA scalar reflectance (top) and changes in DOLP (bottom) when the SSA varies by 0.03 under AOD levels of 0.25 (left), 0.5 (middle), and 1.0 (right) with vegetation surface type.

condition. The magnitudes of ΔI and ΔDOLP decrease as AOD decreases. This highlights that under low AOD conditions, both scalar reflectance and DOLP become less sensitive to SSA, making accurate SSA retrieval more challenging. This also explains why existing remote sensing SSA products can only achieve reasonable accuracy at high AOD levels, and why most validation efforts for SSA products require screening based on an AOD threshold. Consequently, in the following validation sections, the evaluation of SSA results will also be discussed under certain AOD threshold screening conditions.

3.2 Retrieval Experiment Using Simulated Data

The retrieval results on the simulated dataset are shown in Fig. 5. As mentioned in the previous section, the accuracy of retrieved SSA is highly dependent on AOD levels. Therefore, in the validation process, an AOD threshold was applied to filter the retrieved SSA, retaining only those with a 443 nm AOD greater than 0.4 for validation. Overall, the validation results for AOD, SSA, and DHR demonstrate satisfactory performance across all bands, suggesting that the algorithm effectively retrieved these aerosol and surface parameters. Among the three parameters, DHR exhibits the best retrieval performance. The correlation coefficients for 443 nm and 565 nm DHR are both around 0.9, while that for 490 nm DHR reaches 0.77. The biases of the retrieved DHR across the three bands are all within 0.005, with root mean square errors (RMSE) around 0.02. Most retrieval results are distributed near the 1:1 line, and the slopes of the linear regression lines are approximately 0.75, demonstrating a strong linear relationship between the retrieved DHR and the "true values". The retrieved AOD across the three bands also performs well. The retrieved 443 nm AOD achieves a correlation coefficient of 0.85, a bias of -0.008, and an

https://doi.org/10.5194/egusphere-2025-5185
Preprint. Discussion started: 5 December 2025

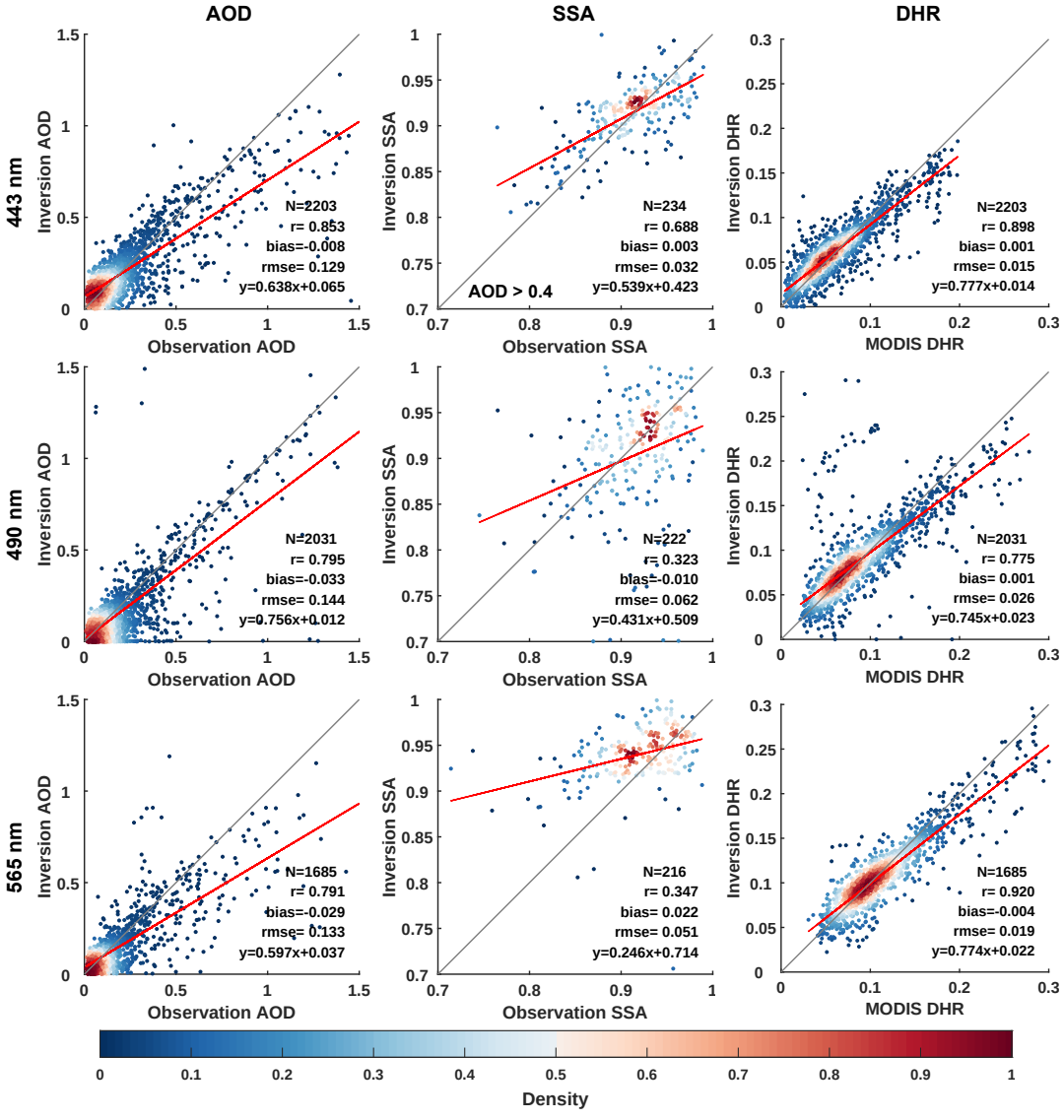

Figure 5. Validation results of AOD (left), SSA(middle), and DHR (Directional Hemispherical Reflectance, right column) at 443 (top), 490 (center), and 565 nm (bottom) using simulated datasets.

RMSE of approximately 0.13 with the "true values". For the other two bands, the correlation coefficients are around 0.8, with biases and RMSEs of approximately -0.03 and 0.14, respectively. The retrieval performance of SSA varies significantly across different wavelengths. For the 443 nm band, the SSA retrieval achieves a correlation coefficient close to 0.7, a bias of only 0.003, and an RMSE of 0.03, meeting the requirements for high-precision SSA retrieval. In contrast, the correlation coefficients for the other two bands range between 0.3 and 0.35, indicating relatively weaker performance.

https://doi.org/10.5194/egusphere-2025-5185
Preprint. Discussion started: 5 December 2025

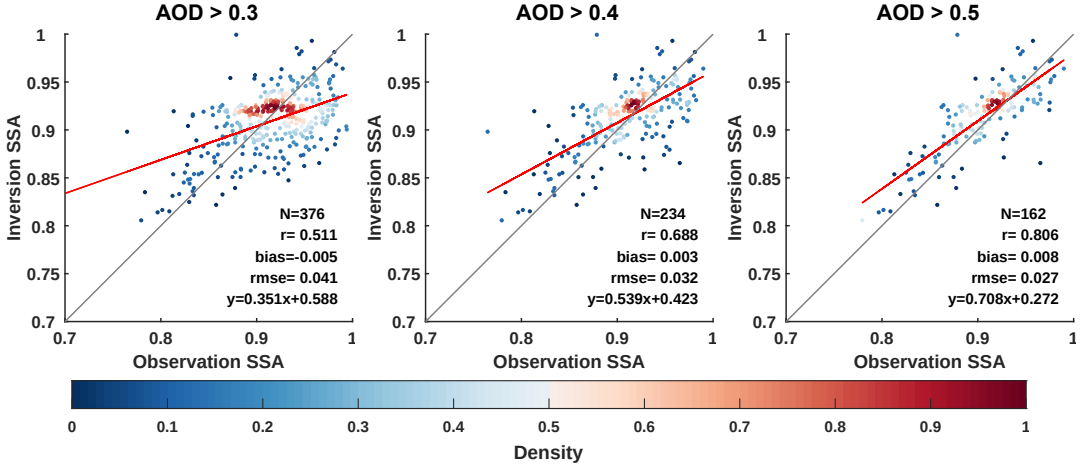

Figure 6. Validation of 443 nm SSA using simulated datasets with AOD thresholds of 0.3 (left), 0.4(middle), and 0.5 (right).

The retrieval performance of the algorithm for AOD, SSA, and DHR is closely related to the sensitivity of the TOA reflectance to these parameters. The sensitivity of TOA reflectance decreases in the order of surface reflectance, AOD, and SSA, leading to a corresponding increase in retrieval uncertainty. Over land surfaces, the contributions of surface and atmosphere to satellite-observed signals are generally of the same order of magnitude (Levy et al., 2007b), resulting in comparable retrieval performance for DHR (representing surface reflectance) and AOD (affecting atmospheric extinction). However, due to the relatively low sensitivity of TOA reflectance to SSA and its dependence on AOD magnitude (Fig. 4), the retrieved SSA exhibits higher uncertainty, which is further influenced by AOD levels. Figure 6 presents the retrieval results for 443 nm SSA under different AOD threshold screenings. The retrieval performance of SSA improves considerably as the AOD threshold increases: the correlation coefficient rises from approximately 0.5 for $AOD_{440} > 0.3$ and to 0.8 for $AOD_{440} > 0.5$, and the slope of the fitted line approaches 1.0 under higher AOD thresholds. These results are consistent with the sensitivity analysis in the previous section. In the following site-based validation process, only an AOD threshold of 0.4 is applied for SSA screening, and the variations in SSA validation results under different AOD thresholds align with those shown in Fig. 6.

Furthermore, the retrieval performance of each parameter varies with wavelength, and the trends differ among the parameters. It is evident that both AOD and SSA exhibit the best retrieval results at the 443 nm band, with slightly weakened performance at 490 nm and 565 nm. In contrast, DHR retrieval performs better at the 565 nm band. These variations are closely related to the wavelength dependence of AOD and surface reflectance. Typically, AOD decreases with increasing wavelength, and Rayleigh scattering by gas molecules also diminishes rapidly at longer wavelengths. Conversely, surface reflectance generally increases with wavelength. As a result, the TOA reflectance at shorter wavelengths contains more atmospheric signals, and the relatively simple Rayleigh scattering signal is easier to separate, leading to better retrieval of AOD and SSA at shorter wavelengths. As the wavelength increases, the surface signal strengthens while the atmospheric signal weakens, resulting in improved surface reflectance retrieval at longer wavelengths but weakened performance for AOD and SSA.

https://doi.org/10.5194/egusphere-2025-5185
Preprint. Discussion started: 5 December 2025

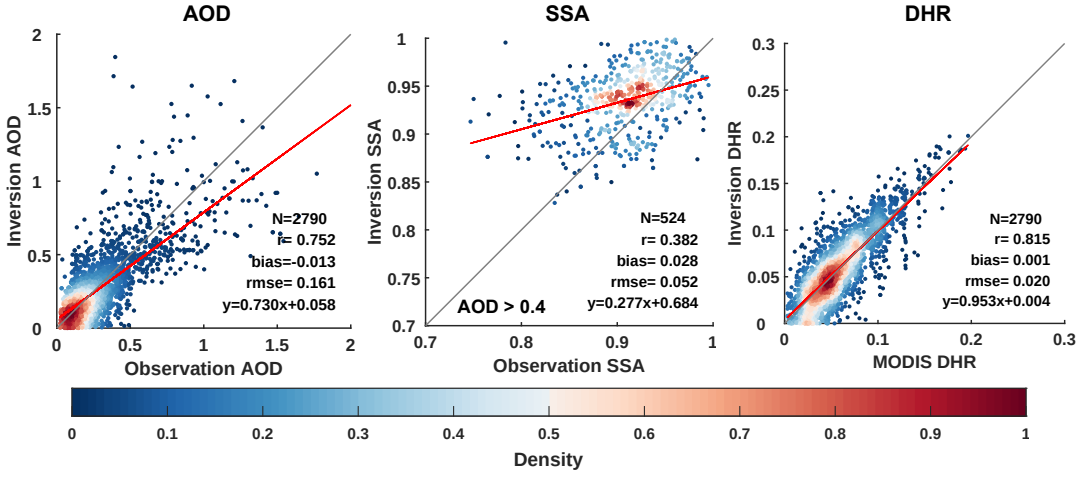

Figure 7. Comparison between retrieved AOD (left), SSA (middle), and DHR (right) at 443 nm based on DPC measurements and AERONET observations.

3.3 Retrieval results on DPC measurements

Validation results from simulated datasets confirm the effectiveness of the inversion algorithm. This section thus further evaluates the performance of the algorithm on DPC measurements and validates the results against AERONET (AOD and SSA) and MODIS (DHR) data. The validation results at 443 nm are shown in Fig. 7. Similar to the retrieval experiment using simulated data, the results at other bands exhibit similar performance to those at 443 nm and are thus not shown here.

Overall, the validation results based on actual DPC observations reasonably agree with those from simulated datasets, demonstrating better performance for DHR and AOD than SSA, consistent with the sensitivity of TOA reflectance to these parameters. Among all results for DPC observations, the retrieved 443 nm DHR and AOD exhibit strong correlations with MODIS and AERONET measurements, respectively. Specifically, DHR achieves a correlation coefficient of 0.81, with a bias and root mean square error (RMSE) of only 0.001 and 0.02 respectively, compared with MODIS observations. AOD achieves a correlation coefficient of 0.75, with a bias of -0.01 and an RMSE of 0.16 compared with AERONET, reaching an accuracy level comparable to the operational MODIS AOD products (Levy et al., 2010) and the machine-learning-based retrievals on DPC reported by Dong et al. (2024). As expected, the SSA retrievals from DPC observations agree less well with AERONET data. For cases with $\mathrm{AOD}_{443} > 0.4$, the retrieved 443 nm SSA yield a correlation coefficient of 0.38, a bias of approximately 0.03, and an RMSE of 0.05, all inferior to the results using simulated data. This discrepancy can be attributed to three main factors. First, SSA retrieval is highly sensitive to observational uncertainties (Zheng et al., 2019). As demonstrated in Sect. 3.1, even at $\mathrm{AOD} > 0.5$, a 0.03 perturbation in SSA induces only a ~ 5 % change of scalar radiance and a less than 0.02 variation of DOLP. However, the actual observational uncertainty of DOLP by DPC may exceed 0.04, and while scalar radiance can be calibrated to reduce systematic errors, its random errors remain significant. The SSA retrieval accuracy is thus inherently limited due to these high observational uncertainties. Moreover, the simulated dataset and retrieval algorithm employed the same radiative

https://doi.org/10.5194/egusphere-2025-5185
Preprint. Discussion started: 5 December 2025

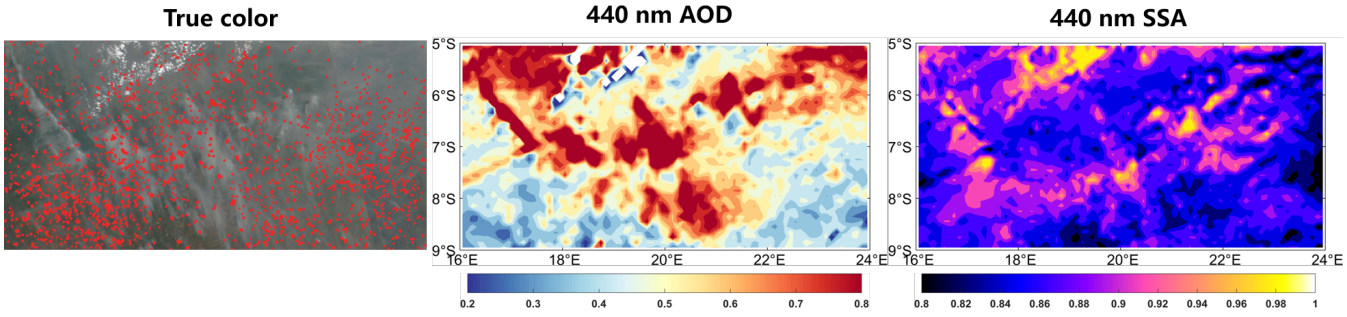

Figure 8. Biomass burning event on July 6, 2019 over southern Africa. (a) True-color image from MODIS and VIIRS. (b) Retrieved 440 nm AOD from DPC observations. (c) Retrieved 440 nm SSA from DPC observations. The true color image is provided by NASA, downloaded from https://worldview.earthdata.nasa.gov/ on 16 June 2025.

transfer model, eliminating additional model uncertainties and enabling higher SSA retrieval precision. In contrast, potential model uncertainties were introduced when applying the algorithm to DPC observations, further reducing SSA retrieval performance. Finally, AERONET SSA measurements themselves have an uncertainty of ~ 0.03, which may also contribute to the degraded SSA validation results.

Nevertheless, current satellite-based SSA retrievals generally exhibit low accuracy. The correlation coefficient of 0.38 in this study is comparable to regional SSA retrievals from DPC observations reported by Fang et al. (2022) and aligns with the precision of POLDER/GRASP SSA products, which have been regarded as the best satellite-based SSA product up to date, with a correlation coefficient of 0.32-0.53 with AERONET measurements (Chen et al., 2020). In summary, the validation results confirm that the retrieval algorithm achieves strong consistency with AERONET and MODIS measurements for AOD and DHR retrievals using DPC observations, while also demonstrating a certain capability for SSA retrieval.

3.4 Retrieval Results during Typical Pollution Events

As discussed previously, the retrieval algorithm demonstrates good performance for AOD retrieval and exhibits certain capability for SSA retrieval under pollution conditions. Therefore, it is promising to identify pollution events and characterize major aerosol types using DPC observations. This section examines the retrieval results for a representative biomass burning and dust event respectively as identified from true-color images from MODIS and VIIRS.

Figure 8 presents the true-color image of a fire event in southern Africa on July 6, 2019, along with the retrieved AOD and SSA from DPC observations. The true-color image reveals dense vegetation and numerous smoke plumes, which should primarily composed of black carbon (BC) and organic carbon (OC) from biomass burning. The AOD retrieval based on DPC observations effectively identifies the spatial distribution of these smoke plumes, highlighting higher aerosol loading in the central, northwestern, and northeastern areas, while lower aerosol concentrations are observed in the southwest and southeast areas. The retrieved AOD also reflects the northwest-southeast orientation of these plumes, demonstrating good detection capability for this pollution event. The retrieved SSA values are mostly low across the region, typically below 0.9, consistent

https://doi.org/10.5194/egusphere-2025-5185
Preprint. Discussion started: 5 December 2025

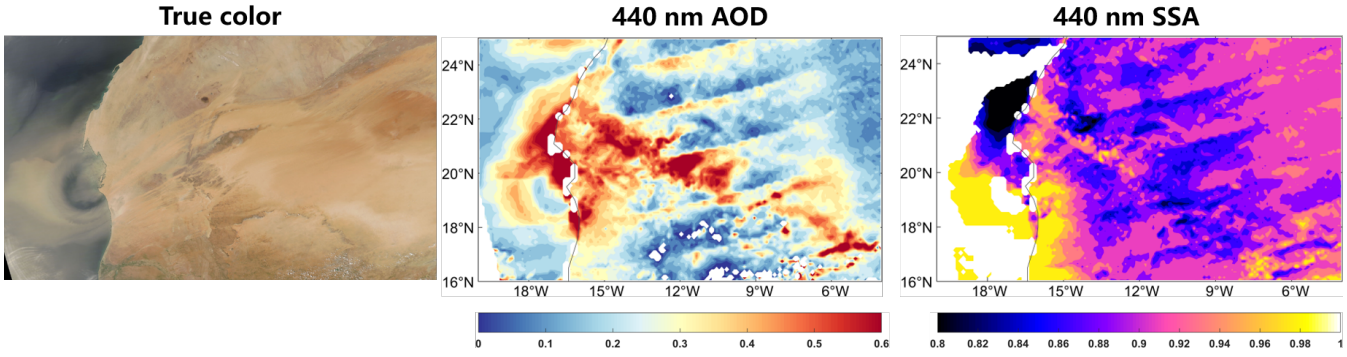

Figure 9. Same as fig. 8, but with dust event on October 2, 2019 over northern Africa. The true color image is provided by NASA, downloaded from https://worldview.earthdata.nasa.gov/ on 16 June 2025.

with the strong absorption properties of biomass burning aerosols, which contain high proportions of BC and/or OC. Moreover, in areas with higher AOD where SSA retrieval uncertainty is reduced, the retrieved SSA values are lower and more coherent, clearly indicating the presence of strongly absorbing aerosol types such as black carbon. Overall, the retrieval results based on DPC observations effectively capture the changes in aerosol loading and absorption for biomass burning events.

Figure 9 presents a dust event in northern Africa on October 2, 2019. The meridional discontinuities in Fig. 9(b,c) primarily originate from inherent observational discontinuities during each cross-track scan of DPC, rather than artifacts of the retrieval algorithm. These discontinuities arise from inaccuracies in satellite geolocation positioning and abrupt changes in viewing geometry between successive cross-track scans. The true-color image shows intense dust activity in the western part of the region, with some dust transported over the ocean. The retrieved AOD from DPC observations effectively captures the high dust loading in this area, particularly the spiral distribution of aerosols over the ocean, which aligns well with the true-color image and indicates the transport of dust from land to sea. The retrieved SSA values in this region are mostly around 0.92, consistent with typical dust SSA. Thus, the retrieval results also successfully identify this dust event.

In summary, the retrieval algorithm demonstrates good capability for identifying the two pollution events by characterizing the loading and absorbing property of biomass burning and dust aerosols. These results provide valuable references for pollution event detection and aerosol type monitoring.

3.5 Global Retrieval Results

To examine the spatiotemporal variability of aerosol and surface parameters, we further investigate the global and seasonal distribution of retrieved parameters. Figures 10–12 show the global distributions of 440 nm AOD, SSA, and land DHR retrieved from DPC observations for April, July, and October 2019, and January 2020, by gridding the pixel level retrievals to a 0.5° grid resolution. The zonal discontinuities in the figures primarily stem from inherent discontinuities in the observational data during the merging of retrieval results from different orbital passes, rather than being introduced by the retrieval algorithm itself.

https://doi.org/10.5194/egusphere-2025-5185
Preprint. Discussion started: 5 December 2025

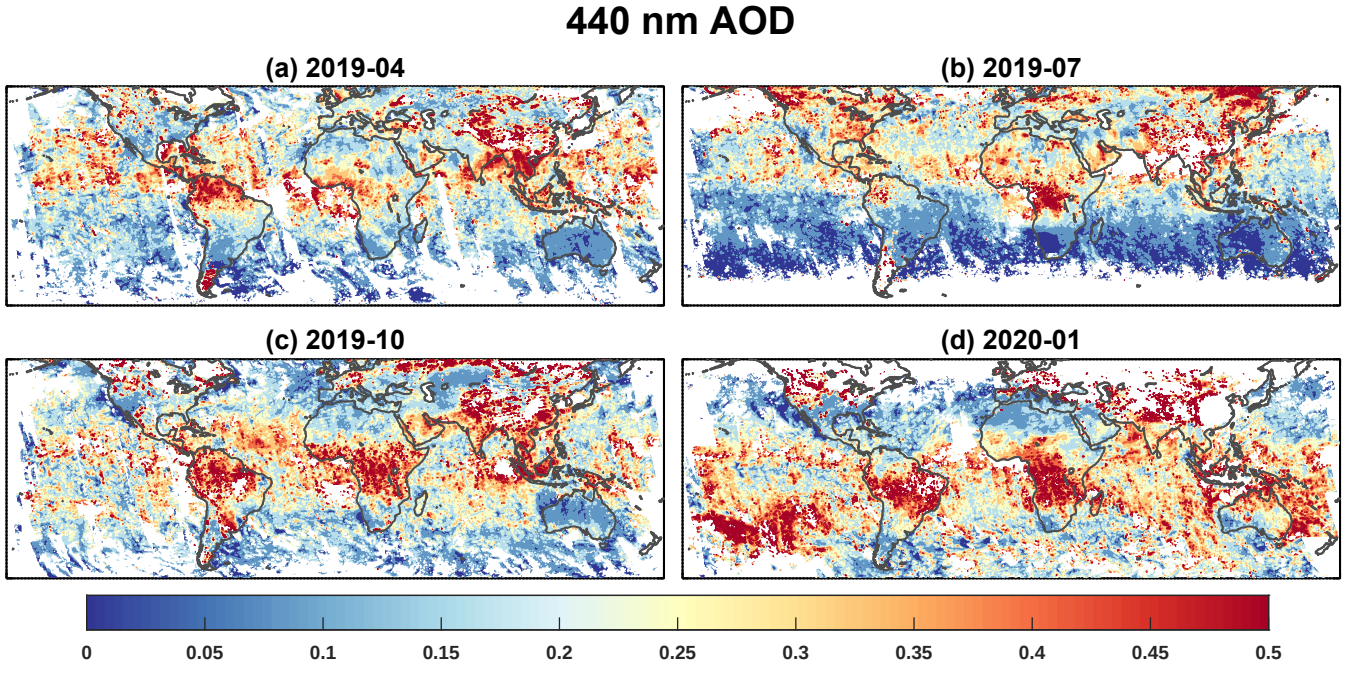

Figure 10. Global 440 nm AOD retrieved from DPC observations.

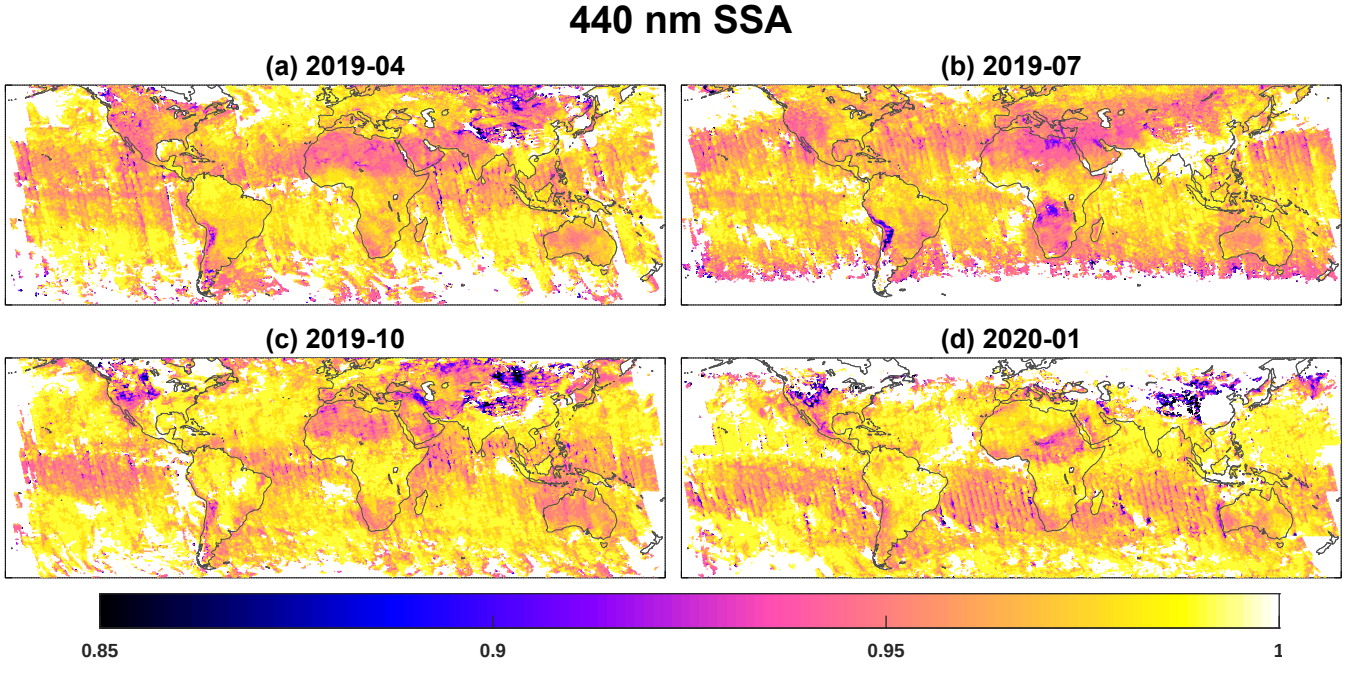

Figure 11. Same as Fig. 10, but for 440 nm SSA.

https://doi.org/10.5194/egusphere-2025-5185
Preprint. Discussion started: 5 December 2025

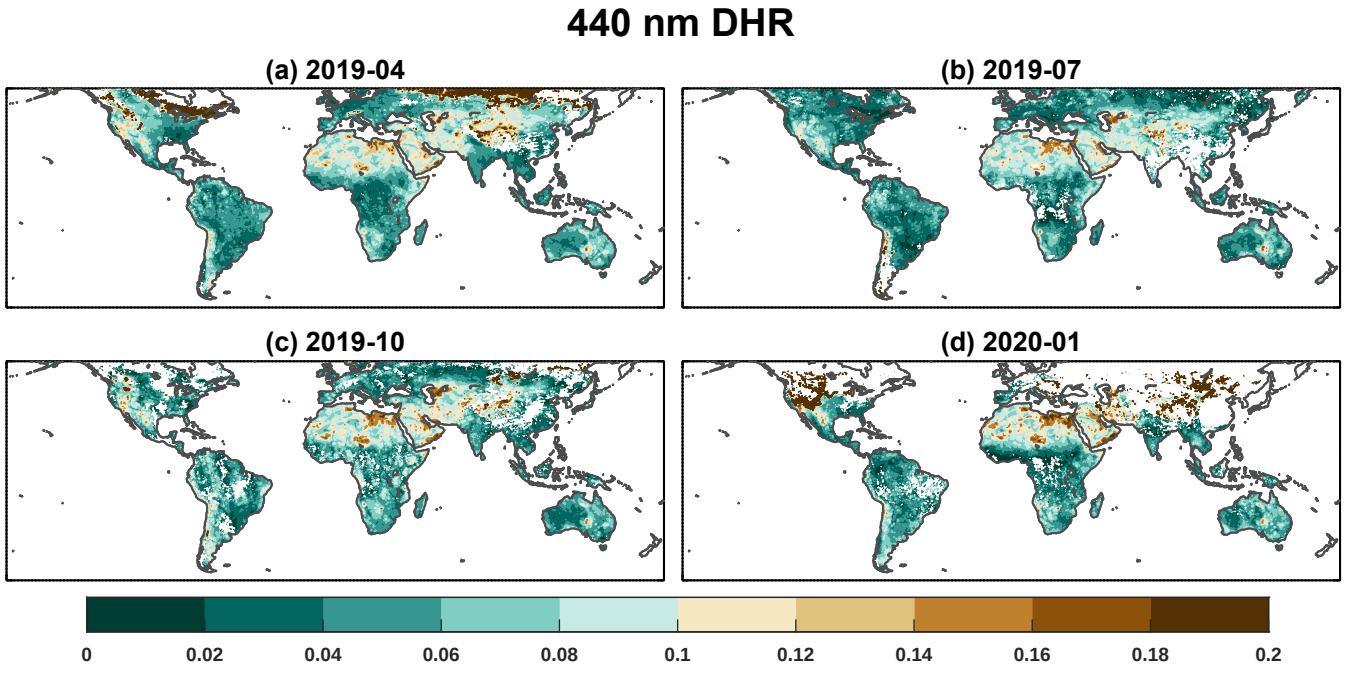

Figure 12. Same as Fig. 10, but for 440 nm DHR.

Overall, the AOD retrievals effectively capture major aerosol source regions (Fig. 10), the spatiotemporal distribution of SSA aligns with regional emission characteristics (Fig. 11), and DHR closely matches local surface types (Fig. 12). The patterns of AOD, SSA, and DHR are highly consistent with other satellite products such as MODIS, OMI, and POLDER (Chen et al., 2020; Heald et al., 2014; Schutgens et al., 2021), and are also in line with previous studies applying DPC observations (Dong et al., 2024).

Specifically, high AOD values are concentrated in the majority of aerosol source regions such as East Asia, South Asia, Africa, the Arabian Peninsula, and northern South America (Fig. 10). Despite using different surface assumptions for land and ocean, the AOD spatial distribution exhibits strong continuity, including the westward transport of Sahara dust in the northern Africa (Engelstaedter et al., 2006) and the spread of aerosols from land to the ocean in pre-monsoon over South Asia (Satheesh and Srinivasan, 2002). The distributions of SSA (Fig. 11) reflect the scattering and absorption properties of aerosols in different regions, highlighting aerosol composition features. Low SSA values are retrieved in Central Asia, Africa, the Arabian Peninsula, central Australia, and western North America, indicating stronger aerosol absorption in these areas. Among these, Central Asia, northern Africa, and the Arabian Peninsula are major dust source regions (Ginoux et al., 2012; Habib et al., 2019), where low SSA is primarily associated with dust emissions. Biomass burning regions in southern Africa, northern South America, western North America, and Australia, also exhibit low SSA values, which are mainly associated with BC and/or OC emissions (Eck et al., 2023; Iglesias et al., 2022; Mallet et al., 2024; Pan et al., 2020; Yang et al., 2021). In

https://doi.org/10.5194/egusphere-2025-5185
Preprint. Discussion started: 5 December 2025

contrast, Europe and eastern North America exhibit higher SSA values due to dominant anthropogenic emissions of scattering-type fine particles (Li et al., 2016; Ramanathan et al., 2001; Wei et al., 2024; Zhang et al., 2025).

The spatial distribution of DHR (Fig. 12) aligns well with local surface types (Yang et al., 2017). Regions such as South America, southern Africa, Europe, Siberia, and eastern North America show lower DHR in summer, reflecting dense vegetation coverage in this season. Conversely, Central Asia, West Africa, and the Arabian Peninsula exhibit higher DHR due to desert surfaces with higher reflectivity. Some regions in western North America and central Australia also exhibit high DHR values, consistent with the drier soil associated with arid climate condition there.

Additionally, the global distributions of AOD, SSA, and DHR across different months effectively capture the seasonal variations in aerosol and surface properties. For instance, high-latitude regions in the Northern Hemisphere exhibit higher DHR in winter than that in summer, reflecting drier conditions and reduced vegetation coverage during winter. In West Africa, intense dust activity during the summer months corresponds to higher AOD (Fig. 10a,b), while AOD is relatively lower in other seasons (Fig. 10c,d). Biomass burning in southern Africa primarily occurs during dry seasons (Mallet et al., 2024; Pan et al., 2020), such as in July when lower SSA values are derived from DPC observations (Fig. 11b). The elevated AOD in northern South America in October (Fig. 10c) is linked to active wildfires during that season (Pan et al., 2020). Notably, while Australia generally exhibits low AOD, significantly higher AOD was observed in January 2020, associated with strong wildfires that began in late 2019. Figure 10d shows the eastward transport of aerosols from Australia, forming a distinct high-AOD band over the Southern Oceans, where SSA also shows lower values. Our DPC retrieval results successfully capture these extreme events.

4 Discussion and Conclusion

Satellite-based retrieval of comprehensive aerosol and surface properties remains a challenging work due to limitations in observational information and the lack of constraints of unknown parameters. Multi-angle polarimetric observations represent a great advancement in this regard, as their great information content enables the retrieval of multiple parameters, including aerosol absorption and surface reflectance (Dubovik et al., 2019). While some studies using DPC observations have demonstrated robust AOD retrievals (Ge et al., 2022; Jin et al., 2022; Wang et al., 2021), progress in SSA retrieval was still quite limited, with no operational global SSA products currently available from DPC observations.

This study developed a numerical algorithm to retrieve global AOD, SSA, and DHR based on DPC observations, achieving results with reasonable accuracy. Our work provides insights into the potential of multi-angle polarimetric observations for the retrieval of aerosol and surface properties, deriving high quality AOD and DHR retrieval and reliable SSA retrieval. The ability to reliably retrieve SSA from space has profound implications for more accurate assessment of aerosol radiative effects and environmental impacts, representing an important advancement in atmospheric remote sensing capabilities. The sensitivity experiments and global-scale results presented here also offer insights into future development of spaceborne multi-angle polarimetric sensors.

https://doi.org/10.5194/egusphere-2025-5185
Preprint. Discussion started: 5 December 2025

The sensitivity analysis of scalar and polarimetric observations to SSA in this work demonstrates that accurate SSA retrieval with an uncertainty of 0.03 requires DOLP observation uncertainties below 0.01 even with optimally designed viewing geometries. The laboratory calibration uncertainty of DPC's DOLP measurements is roughly on par with this requirement (Li et al., 2018), theoretically enabling SSA retrieval. The performance of our algorithm on simulated data further indicates that, within DPC's designed precision, SSA retrieval is feasible, with correlation coefficients between retrieved and "true" 440 nm SSA reaching 0.8 when AOD exceeds 0.5. However, retrieval based on multi-angle polarization observations is highly sensitive to measurement uncertainties (Zheng et al., 2019). Since launch, DPC's optical components have aged, significantly increasing scalar and polarimetric uncertainties (potentially exceeding 10 % for scalar reflectance and 0.04 for DOLP) without effective evaluation or correction methods (Qie et al., 2021; Zhu et al., 2022), which partially explains the difficulty in achieving high-precision SSA retrieval from DPC measurements. In our global validation against AERONET observations, the SSA correlation coefficient reaches approximately 0.38 when 443 nm AOD $>$ 0.4, comparable to the regional retrieval results reported by Fang et al. (2022). The POLDER/GRASP SSA product shows correlation coefficients of 0.32-0.54 for its best-performing 670 nm band when AOD $>$ 0.3 (Chen et al., 2020), also similar to our SSA validation results.

Furthermore, this study derived regional and global distributions of AOD and SSA from DPC observations, along with land surface DHR. Regional results effectively identify pollution events and characterize major aerosol types. The global AOD also reveals major aerosol source regions, while the SSA distribution reflects regional aerosol composition characteristics. The spatial pattern of DHR shows good agreement with local surface types.

In sum, our retrieval results demonstrate the potential of DPC observations for comprehensive aerosol and surface monitoring, despite current limitations in SSA retrieval accuracy. Nonetheless, to an accuracy level of AOD and SSA that meet the requirement of aerosol forcing estimation which requires the uncertainty of SSA to be within 0.03 and that of AOD to be within 10 % (Mishchenko et al., 2004; Loeb and Su, 2010; Zhang et al., 2022), significantly higher quality of scalar and DOLP measurements are needed than the current DPC sensor. The information provided by DPC should thus be considered more qualitative than quantitative. Future improvements in sensor design, calibration, as well as retrieval algorithms may further enhance the precision of aerosol retrievals and provide more quantitative products.

Code and data availability. The AERONET data are available at https://aeronet.gsfc.nasa.gov (last access: 15 October 2025). The MODIS data are available at https://ladsweb.modaps.eosdis.nasa.gov (last access: 15 October 2025). The ERA5 data are available at https://cds.climate.copernicus.eu (last access: 15 October 2025). The salinity data are available at https://ncss.hycom.org/thredds/catalog.html (last access: 15 October 2025). Other data and codes will be made available on request.

Author contributions. JL designed the research. ZZ implemented the research. ZZ and JL wrote the initial draft. YD and CZ helped preprocess the data. YD, CZ, QL, and LG helped collect data and provided guidance in improving the draft.

https://doi.org/10.5194/egusphere-2025-5185
Preprint. Discussion started: 5 December 2025

Competing interests. The authors declare that they have no conflict of interest.

Acknowledgements. We gratefully thank the Chinese National Space Administration Earth Observation and Data Center for providing the DPC/GF-5 data. We appreciate the AEROENT team for supporting the sunphotometers network (https://aeronet.gsfc.nasa.gov/). We also acknowledge NASA for providing MODIS data (https://ladsweb.modaps.eosdis.nasa.gov) and the true-color images used in the article (https://worldview.earthdata.nasa.gov/). This work is funded by National Natural Science Foundation of China Grant No. 42425503, and National Key Research and Development Program of China (Grant 2023YFf0805401).

https://doi.org/10.5194/egusphere-2025-5185
Preprint. Discussion started: 5 December 2025

References

Albrecht, B. A.: Aerosols, Cloud Microphysics, and Fractional Cloudiness, Science, 245, 1227–1230, https://doi.org/10.1126/science.245.4923.1227, 1989.

Chen, C., Dubovik, O., Fuertes, D., Litvinov, P., Lapyonok, T., Lopatin, A., Ducos, F., Derimian, Y., Herman, M., Tanré, D., Remer, L. A., Lyapustin, A., Sayer, A. M., Levy, R. C., Hsu, N. C., Descloitres, J., Li, L., Torres, B., Karol, Y., Herrera, M., Herreras, M., Aspetsberger, M., Wanzenboeck, M., Bindreiter, L., Marth, D., Hangler, A., and Federspiel, C.: Validation of GRASP algorithm product from POLDER/PARASOL data and assessment of multi-angular polarimetry potential for aerosol monitoring, Earth System Science Data, 12, 3573–3620, https://doi.org/10.5194/essd-12-3573-2020, 2020.

Cummings, J. A. and Smedstad, O. M.: Variational Data Assimilation for the Global Ocean, pp. 303–343, Springer Berlin Heidelberg, ISBN 9783642350887, https://doi.org/10.1007/978-3-642-35088-7_13, 2013.

Dai, G., Wu, S., Long, W., Liu, J., Xie, Y., Sun, K., Meng, F., Song, X., Huang, Z., and Chen, W.: Aerosol and cloud data processing and optical property retrieval algorithms for the spaceborne ACDL/DQ-1, Atmospheric Measurement Techniques, 17, 1879–1890, https://doi.org/10.5194/amt-17-1879-2024, 2024.

Diner, D. J., Beckert, J. C., Reilly, T. H., Bruegge, C. J., Conel, J. E., Kahn, R. A., Martonchik, J. V., Ackerman, T. P., Davies, R., and Gerstl, S. A.: Multi-angle Imaging SpectroRadiometer (MISR) instrument description and experiment overview, IEEE Transactions on Geoscience and Remote Sensing, 36, 1072–1087, 1998.

Dong, Y., Li, J., Zhang, Z., Zheng, Y., Zhang, C., and Li, Z.: Machine Learning-Based Retrieval of Aerosol and Surface Properties Over Land From the Gaofen-5 Directional Polarimetric Camera Measurements, IEEE Transactions on Geoscience and Remote Sensing, 62, 1–15, https://doi.org/10.1109/tgrs.2024.3419169, 2024.

Dubovik, O. and King, M. D.: A flexible inversion algorithm for retrieval of aerosol optical properties from Sun and sky radiance measurements, Journal of Geophysical Research: Atmospheres, 105, 20 673–20 696, https://doi.org/10.1029/2000jd900282, 2000.

Dubovik, O., Smirnov, A., Holben, B. N., King, M. D., Kaufman, Y. J., Eck, T. F., and Slutsker, I.: Accuracy assessments of aerosol optical properties retrieved from Aerosol Robotic Network (AERONET) Sun and sky radiance measurements, Journal of Geophysical Research: Atmospheres, 105, 9791–9806, https://doi.org/10.1029/2000jd900040, 2000.

Dubovik, O., Herman, M., Holdak, A., Lapyonok, T., Tanré, D., Deuzé, J. L., Ducos, F., Sinyuk, A., and Lopatin, A.: Statistically optimized inversion algorithm for enhanced retrieval of aerosol properties from spectral multi-angle polarimetric satellite observations, Atmospheric Measurement Techniques, 4, 975–1018, https://doi.org/10.5194/amt-4-975-2011, 2011.

Dubovik, O., Li, Z., Mishchenko, M. I., Tanré, D., Karol, Y., Bojkov, B., Cairns, B., Diner, D. J., Espinosa, W. R., Goloub, P., Gu, X., Hasekamp, O., Hong, J., Hou, W., Knobelspiesse, K. D., Landgraf, J., Li, L., Litvinov, P., Liu, Y., Lopatin, A., Marbach, T., Maring, H., Martins, V., Meijer, Y., Milinevsky, G., Mukai, S., Parol, F., Qiao, Y., Remer, L., Rietjens, J., Sano, I., Stammes, P., Stamnes, S., Sun, X., Tabary, P., Travis, L. D., Waquet, F., Xu, F., Yan, C., and Yin, D.: Polarimetric remote sensing of atmospheric aerosols: Instruments, methodologies, results, and perspectives, Journal of Quantitative Spectroscopy and Radiative Transfer, 224, 474–511, https://doi.org/10.1016/j.jqsrt.2018.11.024, 2019.

Eck, T. F., Holben, B. N., Reid, J. S., Sinyuk, A., Giles, D. M., Arola, A., Slutsker, I., Schafer, J. S., Sorokin, M. G., Smirnov, A., LaRosa, A. D., Kraft, J., Reid, E. A., O'Neill, N. T., Welton, E., and Menendez, A. R.: The extreme forest fires in California/Oregon in 2020: Aerosol optical and physical properties and comparisons of aged versus fresh smoke, Atmospheric Environment, 305, 119 798, https://doi.org/10.1016/j.atmosenv.2023.119798, 2023.

https://doi.org/10.5194/egusphere-2025-5185
Preprint. Discussion started: 5 December 2025

Engelstaedter, S., Tegen, I., and Washington, R.: North African dust emissions and transport, Earth-Science Reviews, 79, 73–100, https://doi.org/10.1016/j.earscirev.2006.06.004, 2006.

Fang, L., Hasekamp, O., Fu, G., Gong, W., Wang, S., Wang, W., Han, Q., and Tang, S.: Retrieval of Aerosol Optical Properties over Land Using an Optimized Retrieval Algorithm Based on the Directional Polarimetric Camera, Remote Sensing, 14, 4571, 2022.

GCOS: The Global Observing System For Climate: Implementation Needs GCOS-200 (GOOS-214), 2016.

Ge, B., Li, Z., Chen, C., Hou, W., Xie, Y., Zhu, S., Qie, L., Zhang, Y., Li, K., and Xu, H.: An Improved Aerosol Optical Depth Retrieval Algorithm for Multiangle Directional Polarimetric Camera (DPC), Remote Sensing, 14, 4045, 2022.

Giles, D. M., Sinyuk, A., Sorokin, M. G., Schafer, J. S., Smirnov, A., Slutsker, I., Eck, T. F., Holben, B. N., Lewis, J. R., Campbell, J. R., Welton, E. J., Korkin, S. V., and Lyapustin, A. I.: Advancements in the Aerosol Robotic Network (AERONET) Version 3 database – automated near-real-time quality control algorithm with improved cloud screening for Sun photometer aerosol optical depth (AOD) measurements, Atmospheric Measurement Techniques, 12, 169–209, https://doi.org/10.5194/amt-12-169-2019, 2019.

Ginoux, P., Prospero, J. M., Gill, T. E., Hsu, N. C., and Zhao, M.: Global-scale attribution of anthropogenic and natural dust sources and their emission rates based on MODIS Deep Blue aerosol products, Reviews of Geophysics, 50, https://doi.org/10.1029/2012rg000388, 2012.

Habib, A., Chen, B., Khalid, B., Tan, S., Che, H., Mahmood, T., Shi, G., and Butt, M. T.: Estimation and inter-comparison of dust aerosols based on MODIS, MISR and AERONET retrievals over Asian desert regions, Journal of Environmental Sciences, 76, 154–166, https://doi.org/10.1016/j.jes.2018.04.019, 2019.

Hasekamp, O. P., Litvinov, P., and Butz, A.: Aerosol properties over the ocean from PARASOL multiangle photopolarimetric measurements, Journal of Geophysical Research: Atmospheres, 116, 2011.

Hasekamp, O. P., Litvinov, P., Fu, G., Chen, C., and Dubovik, O.: Algorithm evaluation for polarimetric remote sensing of atmospheric aerosols, Atmospheric Measurement Techniques, 17, 1497–1525, https://doi.org/10.5194/amt-17-1497-2024, 2024.

Heald, C. L., Ridley, D. A., Kroll, J. H., Barrett, S. R. H., Cady-Pereira, K. E., Alvarado, M. J., and Holmes, C. D.: Contrasting the direct radiative effect and direct radiative forcing of aerosols, Atmospheric Chemistry and Physics, 14, 5513–5527, https://doi.org/10.5194/acp-14-5513-2014, 2014.

Hersbach, H., Bell, B., Berrisford, P., Hirahara, S., Horányi, A., Muñoz-Sabater, J., Nicolas, J., Peubey, C., Radu, R., Schepers, D., Simmons, A., Soci, C., Abdalla, S., Abellan, X., Balsamo, G., Bechtold, P., Biavati, G., Bidlot, J., Bonavita, M., De Chiara, G., Dahlgren, P., Dee, D., Diamantakis, M., Dragani, R., Flemming, J., Forbes, R., Fuentes, M., Geer, A., Haimberger, L., Healy, S., Hogan, R. J., Hólm, E., Janisková, M., Keeley, S., Laloyaux, P., Lopez, P., Lupu, C., Radnoti, G., de Rosnay, P., Rozum, I., Vamborg, F., Villaume, S., and Thépaut, J.: The ERA5 global reanalysis, Quarterly Journal of the Royal Meteorological Society, 146, 1999–2049, https://doi.org/10.1002/qj.3803, 2020.

Holben, B. N., Eck, T. F., Slutsker, I., Tanré, D., Buis, J. P., Setzer, A., Vermote, E., Reagan, J. A., Kaufman, Y. J., Nakajima, T., Lavenu, F., Jankowiak, I., and Smirnov, A.: AERONET—A Federated Instrument Network and Data Archive for Aerosol Characterization, Remote Sensing of Environment, 66, 1–16, https://doi.org/10.1016/S0034-4257(98)00031-5, 1998.

Iglesias, V., Balch, J. K., and Travis, W. R.: U.S. fires became larger, more frequent, and more widespread in the 2000s, Science Advances, 8, https://doi.org/10.1126/sciadv.abc0020, 2022.

Jin, S., Ma, Y., Chen, C., Dubovik, O., Hong, J., Liu, B., and Gong, W.: Performance evaluation for retrieving aerosol optical depth from the Directional Polarimetric Camera (DPC) based on the GRASP algorithm, Atmospheric Measurement Techniques, 15, 4323–4337, 2022.

Jin, S., Ma, Y., Wang, Z., Hong, J., Chen, F., Ti, R., Chen, C., Liu, Z., Zhai, S., and Gong, W.: Retrievals and performance assessment of global marine aerosol optical properties from DPC/GRASP, Journal of Atmospheric and Environmental Optics, 19, 680–697, 2024.

https://doi.org/10.5194/egusphere-2025-5185
Preprint. Discussion started: 5 December 2025

Levy, R. C., Remer, L. A., and Dubovik, O.: Global aerosol optical properties and application to Moderate Resolution Imaging Spectroradiometer aerosol retrieval over land, Journal of Geophysical Research: Atmospheres, 112, D13 210, https://doi.org/10.1029/2006jd007815, 2007a.

Levy, R. C., Remer, L. A., Mattoo, S., Vermote, E. F., and Kaufman, Y. J.: Second-generation operational algorithm: Retrieval of aerosol properties over land from inversion of Moderate Resolution Imaging Spectroradiometer spectral reflectance, Journal of Geophysical Research: Atmospheres, 112, D13 211, https://doi.org/10.1029/2006jd007811, 2007b.

Levy, R. C., Remer, L. A., Kleidman, R. G., Mattoo, S., Ichoku, C., Kahn, R., and Eck, T. F.: Global evaluation of the Collection 5 MODIS dark-target aerosol products over land, Atmospheric Chemistry and Physics, 10, 10 399–10 420, https://doi.org/10.5194/acp-10-10399-2010, 2010.

Levy, R. C., Mattoo, S., Munchak, L. A., Remer, L. A., Sayer, A. M., Patadia, F., and Hsu, N. C.: The Collection 6 MODIS aerosol products over land and ocean, Atmospheric Measurement Techniques, 6, 2989–3034, https://doi.org/10.5194/amt-6-2989-2013, 2013.

Li, J., Li, X., Carlson, B. E., Kahn, R. A., Lacis, A. A., Dubovik, O., and Nakajima, T.: Reducing multisensor satellite monthly mean aerosol optical depth uncertainty: 1. Objective assessment of current AERONET locations, Journal of Geophysical Research: Atmospheres, 121, https://doi.org/10.1002/2016jd025469, 2016.

Li, J., Carlson, B. E., Yung, Y. L., Lv, D., Hansen, J., Penner, J. E., Liao, H., Ramaswamy, V., Kahn, R. A., Zhang, P., Dubovik, O., Ding, A., Lacis, A. A., Zhang, L., and Dong, Y.: Scattering and absorbing aerosols in the climate system, Nature Reviews Earth & Environment, 3, 363–379, https://doi.org/10.1038/s43017-022-00296-7, 2022a.

Li, L., Dubovik, O., Derimian, Y., Schuster, G. L., Lapyonok, T., Litvinov, P., Ducos, F., Fuertes, D., Chen, C., Li, Z., Lopatin, A., Torres, B., and Che, H.: Retrieval of aerosol components directly from satellite and ground-based measurements, Atmospheric Chemistry and Physics, 19, 13 409–13 443, https://doi.org/10.5194/acp-19-13409-2019, 2019.

Li, Z., Hou, W., Hong, J., Zheng, F., Luo, D., Wang, J., Gu, X., and Qiao, Y.: Directional Polarimetric Camera (DPC): Monitoring aerosol spectral optical properties over land from satellite observation, Journal of Quantitative Spectroscopy and Radiative Transfer, 218, 21–37, https://doi.org/10.1016/j.jqsrt.2018.07.003, 2018.

Li, Z., Hou, W., Hong, J., Fan, C., Wei, Y., Liu, Z., Lei, X., Qiao, Y., Hasekamp, O. P., Fu, G., Wang, J., Dubovik, O., Qie, L., Zhang, Y., Xu, H., Xie, Y., Song, M., Zou, P., Luo, D., Wang, Y., and Tu, B.: The polarization crossfire (PCF) sensor suite focusing on satellite remote sensing of fine particulate matter PM2.5 from space, Journal of Quantitative Spectroscopy and Radiative Transfer, 286, 108 217, https://doi.org/10.1016/j.jqsrt.2022.108217, 2022b.

Litvinov, P., Hasekamp, O., and Cairns, B.: Models for surface reflection of radiance and polarized radiance: Comparison with airborne multi-angle photopolarimetric measurements and implications for modeling top-of-atmosphere measurements, Remote Sensing of Environment, 115, 781–792, https://doi.org/10.1016/j.rse.2010.11.005, 2011.

Liu, C., Gao, M., Hu, Q., Brasseur, G. P., and Carmichael, G. R.: Stereoscopic Monitoring: A Promising Strategy to Advance Diagnostic and Prediction of Air Pollution, Bulletin of the American Meteorological Society, 102, E730–E737, https://doi.org/10.1175/bams-d-20-0217.1, 2021.

Loeb, N. G. and Su, W.: Direct Aerosol Radiative Forcing Uncertainty Based on a Radiative Perturbation Analysis, Journal of Climate, 23, 5288–5293, https://doi.org/10.1175/2010jcli3543.1, 2010.

Maignan, F., Bréon, F.-M., Fédèle, E., and Bouvier, M.: Polarized reflectances of natural surfaces: Spaceborne measurements and analytical modeling, Remote Sensing of Environment, 113, 2642–2650, https://doi.org/10.1016/j.rse.2009.07.022, 2009.

https://doi.org/10.5194/egusphere-2025-5185
Preprint. Discussion started: 5 December 2025

Mallet, M., Voldoire, A., Solmon, F., Nabat, P., Drugé, T., and Roehrig, R.: Impact of biomass burning aerosols (BBA) on the tropical African climate in an ocean–atmosphere–aerosol coupled climate model, Atmospheric Chemistry and Physics, 24, 12 509–12 535, https://doi.org/10.5194/acp-24-12509-2024, 2024.

Mishchenko, M., Cairns, B., Kopp, G., Maring, H., Fafaul, B., Knobelspiesse, K., and Chowdhary, J.: Accurate monitoring of terrestrial aerosols and total solar irradiance: The NASA Glory mission, in: 2010 IEEE International Geoscience and Remote Sensing Symposium, pp. 758–760, IEEE, https://doi.org/10.1109/igarss.2010.5652996, 2010.

Mishchenko, M. I. and Travis, L. D.: Light scattering by polydisperse, rotationally symmetric nonspherical particles: Linear polarization, Journal of Quantitative Spectroscopy and Radiative Transfer, 51, 759–778, https://doi.org/10.1016/0022-4073(94)90130-9, 1994.

Mishchenko, M. I., Cairns, B., Hansen, J. E., Travis, L. D., Burg, R., Kaufman, Y. J., Vanderlei Martins, J., and Shettle, E. P.: Monitoring of aerosol forcing of climate from space: analysis of measurement requirements, Journal of Quantitative Spectroscopy and Radiative Transfer, 88, 149–161, https://doi.org/10.1016/j.jqsrt.2004.03.030, 2004.

Mishchenko, M. I., Geogdzhayev, I. V., Rossow, W. B., Cairns, B., Carlson, B. E., Lacis, A. A., Liu, L., and Travis, L. D.: Long-Term Satellite Record Reveals Likely Recent Aerosol Trend, Science, 315, 1543–1543, https://doi.org/10.1126/science.1136709, 2007.

O'Reilly, J. E. and Werdell, P. J.: Chlorophyll algorithms for ocean color sensors - OC4, OC5 & OC6, Remote Sensing of Environment, 229, 32–47, https://doi.org/10.1016/j.rse.2019.04.021, 2019.

Pan, X., Ichoku, C., Chin, M., Bian, H., Darmenov, A., Colarco, P., Ellison, L., Kucsera, T., da Silva, A., Wang, J., Oda, T., and Cui, G.: Six global biomass burning emission datasets: intercomparison and application in one global aerosol model, Atmospheric Chemistry and Physics, 20, 969–994, https://doi.org/10.5194/acp-20-969-2020, 2020.

Popp, T., De Leeuw, G., Bingen, C., Brühl, C., Capelle, V., Chedin, A., Clarisse, L., Dubovik, O., Grainger, R., Griesfeller, J., Heckel, A., Kinne, S., Klüser, L., Kosmale, M., Kolmonen, P., Lelli, L., Litvinov, P., Mei, L., North, P., Pinnock, S., Povey, A., Robert, C., Schulz, M., Sogacheva, L., Stebel, K., Stein Zweers, D., Thomas, G., Tilstra, L., Vandenbussche, S., Veefkind, P., Vountas, M., and Xue, Y.: Development, Production and Evaluation of Aerosol Climate Data Records from European Satellite Observations (Aerosol_cci), Remote Sensing, 8, 421, https://doi.org/10.3390/rs8050421, 2016.

Qie, L., Li, Z., Zhu, S., Xu, H., Xie, Y., Qiao, R., Hong, J., and Tu, B.: In-flight radiometric and polarimetric calibration of the Directional Polarimetric Camera onboard the GaoFen-5 satellite over the ocean, Applied Optics, 60, 7186, https://doi.org/10.1364/ao.422980, 2021.

Ramanathan, V., Crutzen, P. J., Kiehl, J. T., and Rosenfeld, D.: Aerosols, Climate, and the Hydrological Cycle, Science, 294, 2119–2124, https://doi.org/10.1126/science.1064034, 2001.

Satheesh, S. K. and Srinivasan, J.: Enhanced aerosol loading over Arabian Sea during the pre-monsoon season: Natural or anthropogenic?, Geophysical Research Letters, 29, https://doi.org/10.1029/2002gl015687, 2002.

Schaaf, C. B., Gao, F., Strahler, A. H., Lucht, W., Li, X., Tsang, T., Strugnell, N. C., Zhang, X., Jin, Y., Muller, J.-P., Lewis, P., Barnsley, M., Hobson, P., Disney, M., Roberts, G., Dunderdale, M., Doll, C., d'Entremont, R. P., Hu, B., Liang, S., Privette, J. L., and Roy, D.: First operational BRDF, albedo nadir reflectance products from MODIS, Remote Sensing of Environment, 83, 135–148, https://doi.org/10.1016/s0034-4257(02)00091-3, 2002.

Schutgens, N., Dubovik, O., Hasekamp, O., Torres, O., Jethva, H., Leonard, P. J. T., Litvinov, P., Redemann, J., Shinozuka, Y., de Leeuw, G., Kinne, S., Popp, T., Schulz, M., and Stier, P.: AEROCOM and AEROSAT AAOD and SSA study – Part 1: Evaluation and intercomparison of satellite measurements, Atmospheric Chemistry and Physics, 21, 6895–6917, https://doi.org/10.5194/acp-21-6895-2021, 2021.

https://doi.org/10.5194/egusphere-2025-5185
Preprint. Discussion started: 5 December 2025

Sinyuk, A., Dubovik, O., Holben, B., Eck, T. F., Breon, F.-M., Martonchik, J., Kahn, R., Diner, D. J., Vermote, E. F., Roger, J.-C., Lapyonok, T., and Slutsker, I.: Simultaneous retrieval of aerosol and surface properties from a combination of AERONET and satellite data, Remote Sensing of Environment, 107, 90–108, https://doi.org/10.1016/j.rse.2006.07.022, 2007.

Sinyuk, A., Holben, B. N., Eck, T. F., Giles, D. M., Slutsker, I., Korkin, S., Schafer, J. S., Smirnov, A., Sorokin, M., and Lyapustin, A.: The AERONET Version 3 aerosol retrieval algorithm, associated uncertainties and comparisons to Version 2, Atmospheric Measurement Techniques, 13, 3375–3411, https://doi.org/10.5194/amt-13-3375-2020, 2020.

Spurr, R. J.: VLIDORT: A linearized pseudo-spherical vector discrete ordinate radiative transfer code for forward model and retrieval studies in multilayer multiple scattering media, Journal of Quantitative Spectroscopy and Radiative Transfer, 102, 316–342, https://doi.org/10.1016/j.jqsrt.2006.05.005, 2006.

Su, X., Wang, L., Zhang, M., Qin, W., and Bilal, M.: A High-Precision Aerosol Retrieval Algorithm (HiPARA) for Advanced Himawari Imager (AHI) data: Development and verification, Remote Sensing of Environment, 253, 112 221, https://doi.org/10.1016/j.rse.2020.112221, 2021.

Torres, O., Tanskanen, A., Veihelmann, B., Ahn, C., Braak, R., Bhartia, P. K., Veefkind, P., and Levelt, P.: Aerosols and surface UV products from Ozone Monitoring Instrument observations: An overview, Journal of Geophysical Research: Atmospheres, 112, https://doi.org/10.1029/2007jd008809, 2007.

Wang, X., Cai, D., Chen, S., Lou, J., Liu, F., Jiao, L., Cheng, H., Zhang, C., Hua, T., and Che, H.: Spatio-temporal trends of dust emissions triggered by desertification in China, CATENA, 200, 105 160, https://doi.org/10.1016/j.catena.2021.105160, 2021.

Wei, X., Cui, Q., Ma, L., Zhang, F., Li, W., and Liu, P.: Global aerosol-type classification using a new hybrid algorithm and Aerosol Robotic Network data, Atmospheric Chemistry and Physics, 24, 5025–5045, https://doi.org/10.5194/acp-24-5025-2024, 2024.

Yang, B., Zhao, H., and Chen, W.: Semi-empirical models for polarized reflectance of land surfaces: Intercomparison using space-borne POLDER measurements, Journal of Quantitative Spectroscopy and Radiative Transfer, 202, 13–20, https://doi.org/10.1016/j.jqsrt.2017.07.014, 2017.

Yang, X., Zhao, C., Yang, Y., and Fan, H.: Long-term multi-source data analysis about the characteristics of aerosol optical properties and types over Australia, Atmospheric Chemistry and Physics, 21, 3803–3825, https://doi.org/10.5194/acp-21-3803-2021, 2021.

Zhang, L., Li, J., Jiang, Z., Dong, Y., Ying, T., and Zhang, Z.: Clear-Sky Direct Aerosol Radiative Forcing Uncertainty Associated with Aerosol Optical Properties Based on CMIP6 models, Journal of Climate, 35, 3007–3019, https://doi.org/10.1175/jcli-d-21-0479.1, 2022.

Zhang, Z., Li, J., Dong, Y., Zhang, C., Ying, T., and Li, Q.: Long-Term Trends in Aerosol Single Scattering Albedo Cause Bias in MODIS Aerosol Optical Depth Trends, IEEE Transactions on Geoscience and Remote Sensing, 62, 1–9, https://doi.org/10.1109/tgrs.2024.3424981, 2024.

Zhang, Z., Li, J., Che, H., Dong, Y., Dubovik, O., Eck, T., Gupta, P., Holben, B., Kim, J., Lind, E., Saud, T., Tripathi, S. N., and Ying, T.: Long-term trends in aerosol properties derived from AERONET measurements, Atmospheric Chemistry and Physics, 25, 4617–4637, https://doi.org/10.5194/acp-25-4617-2025, 2025.

Zheng, F., Hou, W., and Li, Z.: Optimal estimation retrieval for directional polarimetric camera onboard Chinese Gaofen-5 satellite: an analysis on multi-angle dependence and a posteriori error, Acta Physica Sinica, 68, 040 701, https://doi.org/10.7498/aps.68.20181682, 2019.

Zhu, S., Li, Z., Qie, L., Xu, H., Ge, B., Xie, Y., Qiao, R., Xie, Y., Hong, J., Meng, B., Tu, B., and Chen, F.: In-Flight Relative Radiometric Calibration of a Wide Field of View Directional Polarimetric Camera Based on the Rayleigh Scattering over Ocean, Remote Sensing, 14, 1211, https://doi.org/10.3390/rs14051211, 2022.